

Basin Entropy, a Measure of Final State Unpredictability and Its Application to the Chaotic Scattering of Cold Atoms

Alvar Daza, Alexandre Wagemakers, Bertrand Georgeot,
David Guéry-Odelin and Miguel A.F. Sanjuán

1 Introduction to Basin Entropy

Dynamical systems describe quantities evolving in time according to deterministic rules, and towards some asymptotic behavior depending on the initial conditions and on the specific choice of parameters. Basins of attraction link a given set of initial conditions to its corresponding final states. This notion appears in a broad range of applications where several outcomes are possible, which is a common situation in neuroscience, economy, astronomy, ecology and many other disciplines. Depending on the nature of the basins, prediction can be difficult even in systems that evolve under deterministic rules. From this respect, a proper classification of this unpredictability is clearly required. To address this issue, we introduce the basin entropy, a measure to quantify this uncertainty.

A. Daza (✉) · A. Wagemakers · M.A.F. Sanjuán
Nonlinear Dynamics, Chaos and Complex Systems Group, Departamento de Física,
Universidad Rey Juan Carlos, Tulipán s/n, 28933 Móstoles, Madrid, Spain
e-mail: alvar.daza@urjc.es

A. Wagemakers
e-mail: alexandre.wagemakers@urjc.es

M.A.F. Sanjuán
e-mail: miguel.sanjuan@urjc.es

B. Georgeot
Laboratoire de Physique Théorique, IRSAMC, Université de Toulouse,
CNRS, UPS, Toulouse, France
e-mail: bertrand.georgeot@irsamc.ups-tlse.fr

D. Guéry-Odelin
Laboratoire Collisions, Agrégats, Réactivité, IRSAMC, Université de Toulouse,
CNRS, UPS, Toulouse, France
e-mail: dgo@irsamc.ups-tlse.fr

M.A.F. Sanjuán
Institute for Physical Science and Technology, University of Maryland,
College Park, MD 20742, USA

1.1 *Final State Unpredictability in Dynamical Systems*

Imagine a rainy day. A droplet falls in the ground and runs until it eventually reaches a river. Another droplet falls nearby, but in its run towards the lowest point, it ends in a different mass of water, a lake for example. If we were to determine the fate of each falling droplet, we should study the regions leading to each mass of water, that is, we should study their different basins. This picture explains perfectly the origin of the term basin in nonlinear dynamics: a basin is the set of initial conditions leading to a particular region of phase space [1]. Dynamical systems specify the evolution of some magnitudes in time according to deterministic rules, in a similar way as the profile of the ground determines the path of streams of water. In dissipative systems, the final destination is typically an attractor, in open Hamiltonian systems, the particular region of phase space usually refers to an exit.

If a given dynamical system has only one attractor or exit, then the fate of any initial condition is clearly determined. However, dynamical systems often present several possible final outcomes and, in these cases of multistability, elucidating which orbits tend to which attractor becomes a fundamental question. For instance, if a system has two attractors, then two basins exist separated by a basin boundary. This basin boundary can be a smooth curve or can be instead a fractal curve. The study of these basins can provide much information about the system since their topology is deeply related to the dynamical nature of the system. For example, systems with chaotic dynamics usually display basins of attraction with fractal structures [2].

In order to give an intuitive picture of our problem we may look at Fig. 1a and b. The figures show the escape basins of the Hénon-Heiles Hamiltonian for two different values of the energy E above the critical energy that separates bounded motions from unbounded motions. Most initial conditions leave the region through one of the three different exits to infinity for any E above this critical energy. The colors represent points that taken as initial conditions leave the region through a specific exit. With this in mind, we may intuitively understand that it is harder to predict in advance which will be the final destination of an orbit in Fig. 1a than in Fig. 1b.

The problem is that even though, we can have an intuitive notion that Fig. 1a is more uncertain than Fig. 1b, there is no quantitative measure to affirm this. Moreover, this is not easy to assess when we compare two figures of basins corresponding to close values of the energy.

This is precisely the idea of uncertainty or unpredictability which we are considering here. This remark is important since we are aware that these terms are polysemic and consequently its use in the literature might be confusing. Here we refer to unpredictability or uncertainty as the difficulty in the determination of the final state of a system, that is, to which attractor the initial conditions will tend to. Note that we speak about attractors for simplicity, though the discussion is identical for open Hamiltonian systems, where there are no attractors. This notion of unpredictability strongly differs from others used in nonlinear dynamics, like the Kolmogorov-Sinai entropy [3, 4], the topological entropy [5], or the expansion entropy [6], which refer to the difficulty of predicting the evolution of the trajectories. All these quantities

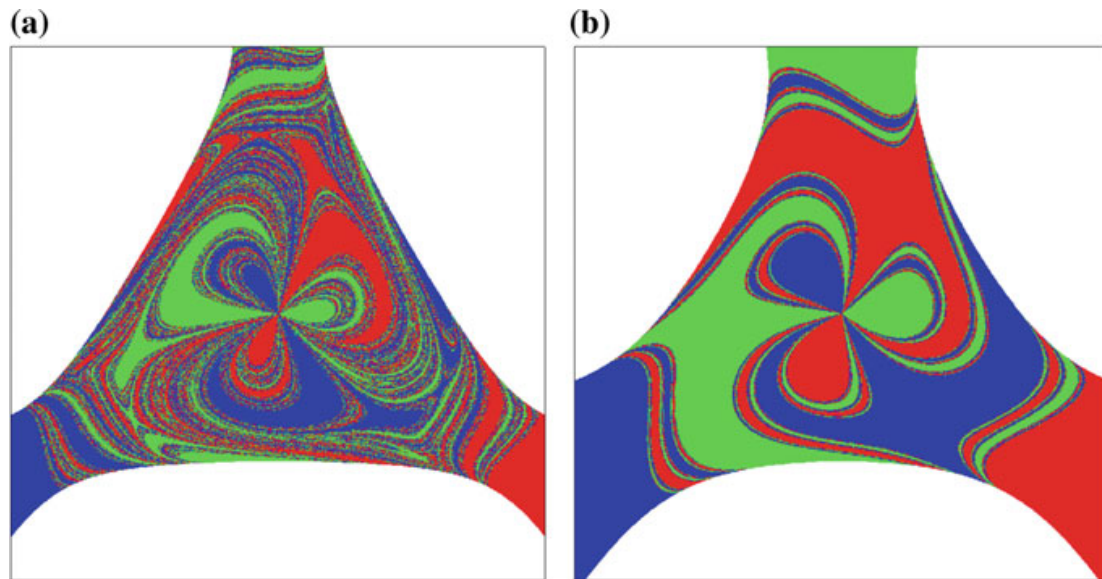


Fig. 1 Comparison between basins. Escape basins for the Hénon-Heiles system but different energies. They represent which exit will take each initial condition. It is clear that determining the final destination of the trajectories in the case (a) is harder than in the case (b)

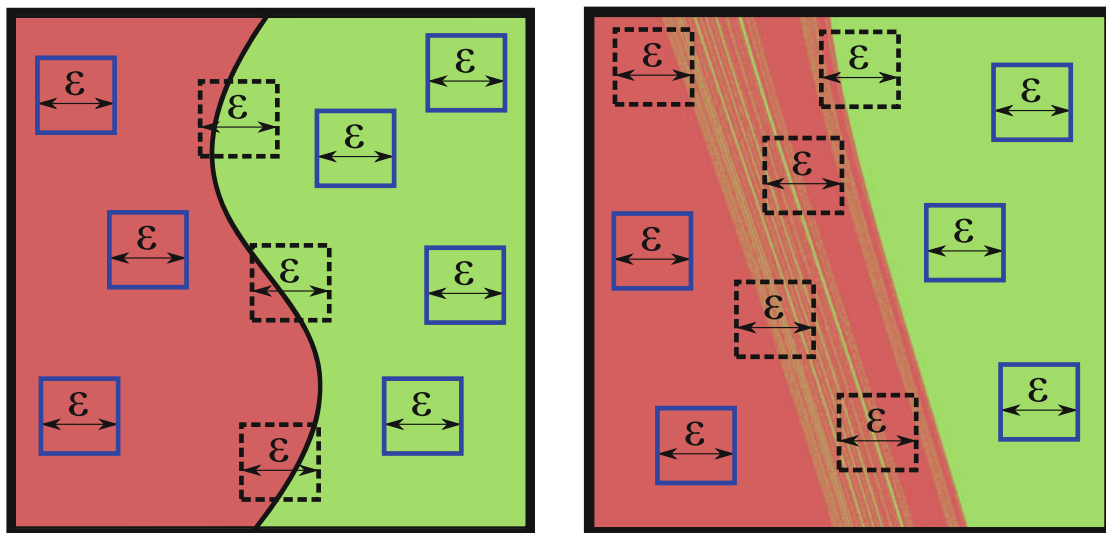


Fig. 2 Uncertainty in the basin boundaries. Given some uncertainty in the initial conditions ε , the final state of a dynamical system depends on the structure of its basins. In the left panel, two basins separated by a smooth boundary. In the right panel, two basins separated by fractal boundaries. The black-dashed boxes are for uncertain initial conditions (boxes intersecting the basin boundary)

are related to the topology of the trajectories, whereas our aim here is to develop an entropy depending on the topology of the basins.

A first approach to study the final state uncertainty in dynamical systems was investigated by Grebogi et al. [7]. Given two attractors, they studied how the predictability of the system depends on the fractal or smooth nature of the basin boundaries. Let us describe their methodology by looking at Fig. 2. In the picture, we can see two different basins (red and green) leading to two different final destinations.

Now consider that the initial conditions have some error or that they suffer a small perturbation of size ε , a situation which is always unavoidable in practice. Therefore, instead of considering initial conditions as points, we rather consider them as boxes of linear size ε . If we study the evolution of many of these boxes of initial conditions, we can find out the ratio f of boxes whose future is uncertain, in the sense that not all the initial conditions within the box will end in the same attractor. These boxes are represented by a black dashed line in Fig. 2, and we would have $f = 3/10$ for the left panel and $f = 5/10$ for the right one. Coming back to our analogy, we are counting how many droplets fall in the boundary between basins in this rain of initial conditions. If we vary the size of the boxes ε , we can find that for smooth boundaries the ratio of uncertain initial conditions f grows linearly with ε . However, for fractal boundaries, the ratio of uncertain initial conditions is $f \sim \varepsilon^\alpha$, where α is the dimension of the phase space D minus the capacity dimension d of the boundary that separates both basins

$$\alpha = D - d. \quad (1)$$

This quantity α is called the uncertainty exponent, and we have $\alpha = 1$ for smooth boundaries whilst $\alpha < 1$ for basins with fractal boundaries. The closer α gets to zero the more difficult it becomes to predict the system as we zoom in. In cases where smooth and fractal basins are mixed, the uncertainty exponent can still be calculated for each boundary. However, the procedure in these cases is cumbersome [8].

A different approach to measure the unpredictability by means of its basins consists of evaluating the volume of each basin in a certain region of phase space. The ratio of the volume occupied by a single basin to the total volume defines the basin stability [9]. It aims at classifying the different basins according to their relative sizes: larger basins are considered more stable (in our picture, the larger the basin the more droplets will fall into it). Although the basin stability may shed some light into problems related to networks of coupled oscillators, it does not take into account the morphology of the basins, but only their volume. For different sets of parameters, two basins can show smooth or fractal boundaries while the volume of each basin remains constant. The basin stability would be the same in both cases but obviously fractal boundaries have a more complex structure and thus, the final state predictability is not the same.

Figure 3 reveals the limitations of both basin stability and the uncertainty exponent α . The four basins have the same basin stability (the proportion of red and green is the same in the four pictures) although they are clearly different. The uncertainty exponent also fails to capture the uncertainty associated to these basins: it cannot distinguish among different smooth boundaries or among different riddled boundaries [10–12]. However, the basin entropy [13] takes increasing values for each basin, matching our intuition. In the following we introduce the mathematical definition of the basin entropy and a method for its computation.

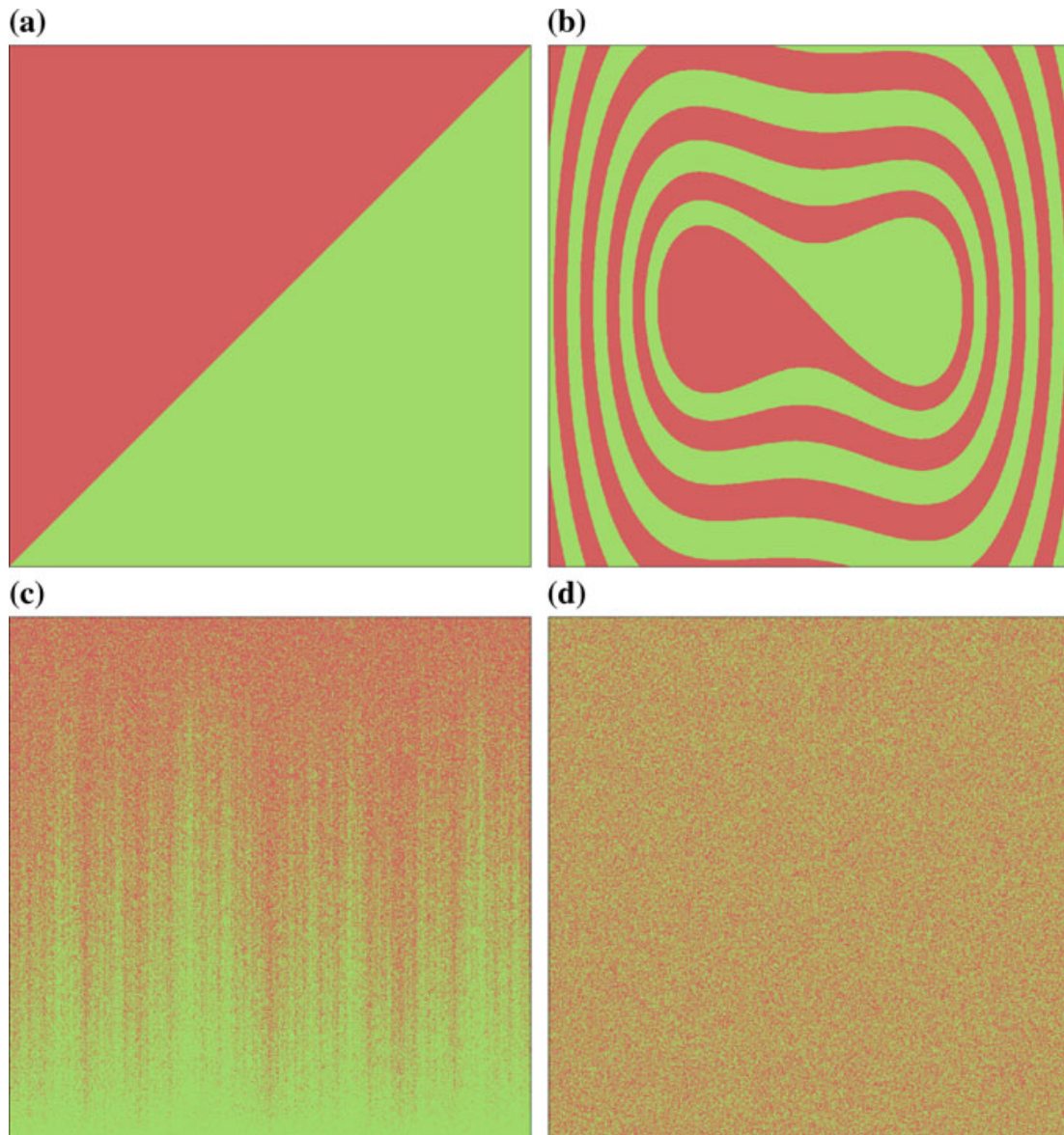


Fig. 3 Comparison of basins and the methods to characterize them. The figure shows different basins obtained from well-known dynamical systems with two attractors. In the two upper panels, the uncertainty exponent is $\alpha = 1$ since both boundaries are smooth, while for the two lower panels $\alpha = 0$ since both of them are riddled basins. The basin stability is equal to $1/2$ for the four basins. However, the basin entropy is able to distinguish the four cases and provides a method to measure quantitatively the unpredictability in increasing order from (a) to (d)

1.2 Definition and Computation of the Basin Entropy

Suppose we have a dynamical system with N_A possible final outcomes for a choice of parameters in a certain region Ω of the phase space. We can discretize Ω via a finite number of boxes covering it, or sample Ω randomly using a sufficient number of boxes. Here we study two-dimensional phase spaces, so that we cover Ω with boxes of linear size ε . Now we build an application relating each initial condition to

its final destination, so that we will refer to that application as the *color*. Each box contains in principle infinitely many trajectories, each one leading to a color labeled from 1 to N_A . In practice we can use only a finite number of trajectories per box. We will discuss this point later in relation with an experimental setup used in the scattering of cold atoms.

Although ε is our limiting resolution, the information provided by the trajectories inside a box can be used to make hypotheses on the uncertainty associated to the box. We consider the colors into the box distributed at random according to some proportions. We can associate a probability to each color j inside a box i as $p_{i,j}$ which will be evaluated by computing statistics over the trajectories inside the box.

Taking into account that the trajectories inside a box are independent in a statistical sense, the Gibbs entropy of every box i is given by

$$S_i = - \sum_{j=1}^{m_i} p_{i,j} \log(p_{i,j}), \quad (2)$$

where $m_i \in [1, N_A]$ is the number of colors inside the box i , and the probability $p_{i,j}$ of each color j is determined simply by the number of trajectories leading to that color divided by the total number of trajectories in the box. Finally, using a sufficient number of boxes N we can define the basin entropy as the mean value of the entropy for those boxes:

$$S_b = \sum_{i=1}^N \frac{S_i}{N}. \quad (3)$$

An interpretation of this quantity is associated to the degree of uncertainty of the basin, ranging from 0 (a sole attractor) to $\log N_A$ (completely randomized basins with N_A equiprobable attractors). This latter upper value is in practice seldom realized even for extremely chaotic systems. It is important to remark that the basin entropy depends on the scaling box size ε , i.e., the basin entropy is an extensive property. Therefore, to make quantitative comparisons of different basins we must fix ε .

The procedure for the calculation of the basin entropy is quite similar to the procedure used for the determination of the uncertainty exponent. However, there are important differences. The first one is that when we compute the basin entropy we use the information contained in the boxes. We do not just label the boxes as certain or uncertain like for the uncertainty exponent, but we study the probabilities of the different outcomes through the proportions of different colors inside each box. The second important difference is that, as we will show later, we do not need different scales ε to compare the uncertainty of different basins. Even more, we can detect fractal structures using only one scale. This is fundamental to study the final state unpredictability in experimental systems with finite resolution, like the beam splitter for cold atoms described later.

1.3 What Does the Basin Entropy Measure?

At this point, we can delve deeper into the consequences of this definition by considering a simple hypothesis, which is to assume that the colors inside a box are equiprobable, thus $p_{i,j} = 1/m_i, \forall j$. If we add the entropy of all the trajectories in a box, then we recover the Boltzmann expression for the entropy $S_i = \log(m_i)$, where m_i are the different colors inside a box (the accessible microstates of the Boltzmann entropy). Then the equiprobable total entropy becomes $S = \sum_{i=1}^N S_i = \sum_{i=1}^N \log(m_i)$. Furthermore, if we have a grid on a given region of phase space, many boxes will have an equal number of colors. That is, many boxes will be in the interior or lie near the boundary between two or more basins. Then we can say that there are N_k equal boxes (in the sense that they have the same number of colors), where $k \in [1, k_{max}]$ is the label for the different boundaries. Boxes lying outside the basin boundaries do not contribute to the entropy as they only have one color. In other words, what matters is what happens at the basin boundaries. Then, the basin entropy reads

$$S_b = \sum_{k=1}^{k_{max}} \frac{N_k}{N} \log(m_k). \quad (4)$$

By following the method of the box-counting dimension D_k [14], by which we compute fractal dimensions of basin boundaries, the number of boxes that contains a boundary grows like $N_k = n_k \varepsilon^{-D_k}$ where n_k is a positive constant. In the case of smooth boundaries, the equation $D_k = D - 1$ holds, D being the dimension of the phase space. For fractal boundaries D_k can be larger, but obviously we always have $D_k \leq D$. On the other hand, the number of boxes in the whole region of phase space, grows as $N = \tilde{n} \varepsilon^{-D}$, where \tilde{n} is a positive constant. Substituting these expressions for N_k and N in Eq. 4, and recalling that $\alpha_k = D - D_k$ is the uncertainty exponent [7] for each boundary, we get

$$S_b = \sum_{k=1}^{k_{max}} \frac{n_k}{\tilde{n}} \varepsilon^{\alpha_k} \log(m_k). \quad (5)$$

This last expression reveals important information. The basin entropy has three components: the term n_k/\tilde{n} is a normalization constant that accounts for the boundary size which is independent of ε ; the term of the uncertainty exponent α_k , is related with the fractality of the boundaries and contains the variation of the basin entropy with the box size; finally there is a term that depends on the number of different colors m_k . All these terms depend on the dynamics of the system, while the scaling box size ε depends only on the geometry of the grid.

Equation 5 sheds light into some interesting questions. First, we can compare smooth boundaries ($\alpha_k = 1$) and fractal boundaries ($\alpha_k < 1$). For both of them, smooth and fractal basins, we get $S_b \rightarrow 0$ when $\varepsilon \rightarrow 0$, but it converges faster in the smooth case. That is, it is more difficult for the basin entropy to decrease its value in

a system with fractal boundaries. Despite other important factors, fractal boundaries introduce a larger uncertainty than the smooth ones. Furthermore, if $\alpha_k = 0$ then $S_b > 0$ no matter the scaling box size (this might happen in riddled basins [10–12]).

These ideas can be successfully applied for Wada basins. Basins exhibiting the Wada property have only one boundary that separates all the basins [15, 16]. We can argue that increasing the number of colors in the boundary boxes increases the basin entropy and therefore its uncertainty. In particular, having all possible colors in every boundary box is a unique situation found only in Wada basins. Nevertheless, Eq. 5 also reveals that some non-Wada basins can show larger basin entropy than others exhibiting the Wada property. This can be the case when a system has the Wada property but there is one basin which occupies most of the phase space. Other factors like the number of attractors and the boundary size also play a role in the uncertainty according to the basin entropy formulation. Therefore the Wada property increases the uncertainty under the basin entropy perspective, but each case must be carefully studied.

1.4 Numerical Examples to Help Understand the Basin Entropy

Here we illustrate the main features of basin entropy with several examples of dynamical systems, showing how its dependence on the boundary size n_k/\tilde{n} , the uncertainty exponent α_k and the number of attractors N_A .

The term n_k/\tilde{n} corresponds to an estimate of the size of the boundary, since it normalizes the number of boxes containing the boundaries divided by the total number of boxes covering Ω :

$$\frac{N_k}{N} = \frac{n_k}{\tilde{n}} \varepsilon^{\alpha_k}. \quad (6)$$

To study the contribution of this term, we consider the damped Duffing oscillator given by

$$\ddot{x} + \delta\dot{x} - x + x^3 = 0. \quad (7)$$

This equation describes the motion of a unit mass particle in a double well potential with dissipation. This system presents two attractive fixed points in $(\pm 1, 0)$ of the (x, \dot{x}) phase space, which correspond to the minima of the double well potential function. The higher the damping coefficient δ the faster the orbits tend to the fixed points and, as a consequence, the basin of attraction appears more deformed for smaller values of δ (Fig. 4a–c). The damped Duffing oscillator is bistable, $N_A = 2$, and has a smooth boundary with uncertainty exponent $\alpha = 1$.

Observing the basins of attraction corresponding to the three different values of δ , it is noticeable that the basin of Fig. 4c has a much simpler structure than the basin in Fig. 4a. The outcome of an initial condition within an ε -box would be more difficult

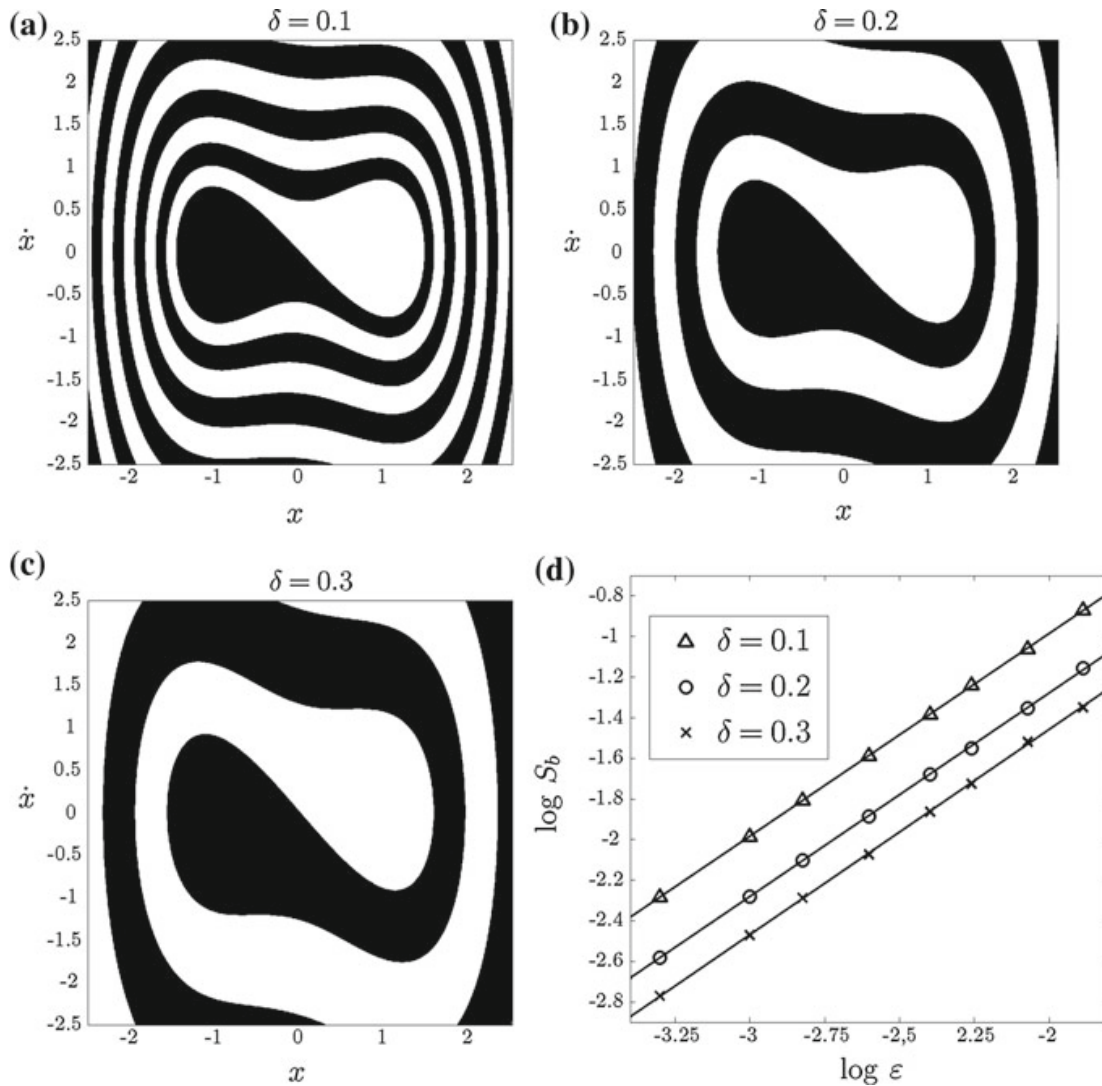


Fig. 4 Basin entropy dependence on the boundary size. a–c Basins of attraction of the damped Duffing oscillator (Eq. 7) for different values of the damping coefficient δ . As the damping increases the boundary occupies a smaller region of the phase space. Although the boundary is always smooth ($\alpha = 1$), the uncertainty in basin (a) is larger than in basin (c) no matter the scaling box size ϵ . d A log-log plot of the basin entropy versus the scaling box size for values of the damping coefficient $\delta = 0.1$ (triangles), $\delta = 0.2$ (circles) and $\delta = 0.3$ (crosses). The three fits have the same slope $\alpha = 1$ within statistical error. However, the basin entropy is different for each value of the parameter δ , reflecting the different uncertainty associated to each basin

to predict in the second case. Nevertheless, both basins have the same uncertainty exponent $\alpha = 1$ since in both cases the boundary is smooth. The differences in the values of the basin entropy originates from the differences in the region of discretized phase space occupied by the boundary, that is, the boundary size, which is reflected by the term n/\tilde{n} (indices have been dropped since now there is only one boundary).

In order to highlight this effect, we have computed the basin entropy S_b versus the scaling box size¹ ε for three different values of the damping coefficient δ . The results are shown in the log-log plot of Fig. 4d, where each fit corresponds to a different value of δ . In order to interpret these results, we can take logarithms on both sides of Eq. 5 yielding to

$$\log(S_b) = \alpha \log(\varepsilon) + \log\left(\log(N_A) \frac{n}{\tilde{n}}\right). \quad (8)$$

Since in this case, we have $\alpha = 1$ and $N_A = 2$ for all our simulations, it is clear that the variation of the basin entropy with δ is entirely due to the term n/\tilde{n} . Most importantly, we have obtained values of the slope $\alpha = 1$ within the statistical error for all the fits. Therefore, although all these basins have the same uncertainty exponent, they have a different basin entropy for a given value of ε . The basin entropy is sensitive to their different structure and is able to quantify their associated unpredictability.

The fractal dimension of the boundaries also plays a crucial role in the formulation of the basin entropy. This is reflected in the uncertainty exponent α_k [7] of Eq. 5. In order to highlight the effects of the variations in the uncertainty exponent, we have chosen a model that can display the Wada property [17]. This means that there is only one fractal boundary separating all the basins. The model is the Hénon-Heiles Hamiltonian [18],

$$H = \frac{1}{2}(\dot{x}^2 + \dot{y}^2) + \frac{1}{2}(x^2 + y^2) + x^2y - \frac{1}{3}y^3, \quad (9)$$

which describes the motion of a particle in an axisymmetrical potential well that for energy values above a critical one, the trajectories may escape from the bounded region inside the well and go on to infinity through three different exits. For this Hamiltonian system, we define escape basins in a similar way to the basins of attraction in dissipative systems, i.e., an escape basin is the set of initial conditions that lead to a certain exit. If we vary the energy from $E = 0.2$ to $E = 0.22$, the fractal dimension of the boundaries is modified with E , though the Wada property is preserved [19] (see Fig. 5a–c). The proportion of red, blue and green remains as a constant for these three basins, leading to constant values of the basin stability. However, the basin entropy accounts for their different structures.

As we compute the basin entropy for different scaling box sizes, we observe that the main effect of varying the parameter E is a change of the slope in the log-log plot of Fig. 5d. Equation 8 relates these changes in the slope to the uncertainty exponent α of the boundary. Smaller energies lead to smaller uncertainty exponents, since the boundaries have a more complex structure and consequently the slopes in the log-log plot also decrease. Obviously the offset also varies for the different values of the energy. This is related to changes in the boundary size n/\tilde{n} which in this case cannot be completely separated from the changes in α . This example shows that the

¹In this work we have normalized the region of the phase space, so that the values of the scaling box size ε in the plots are the inverse of the number of pixels used as a grid.

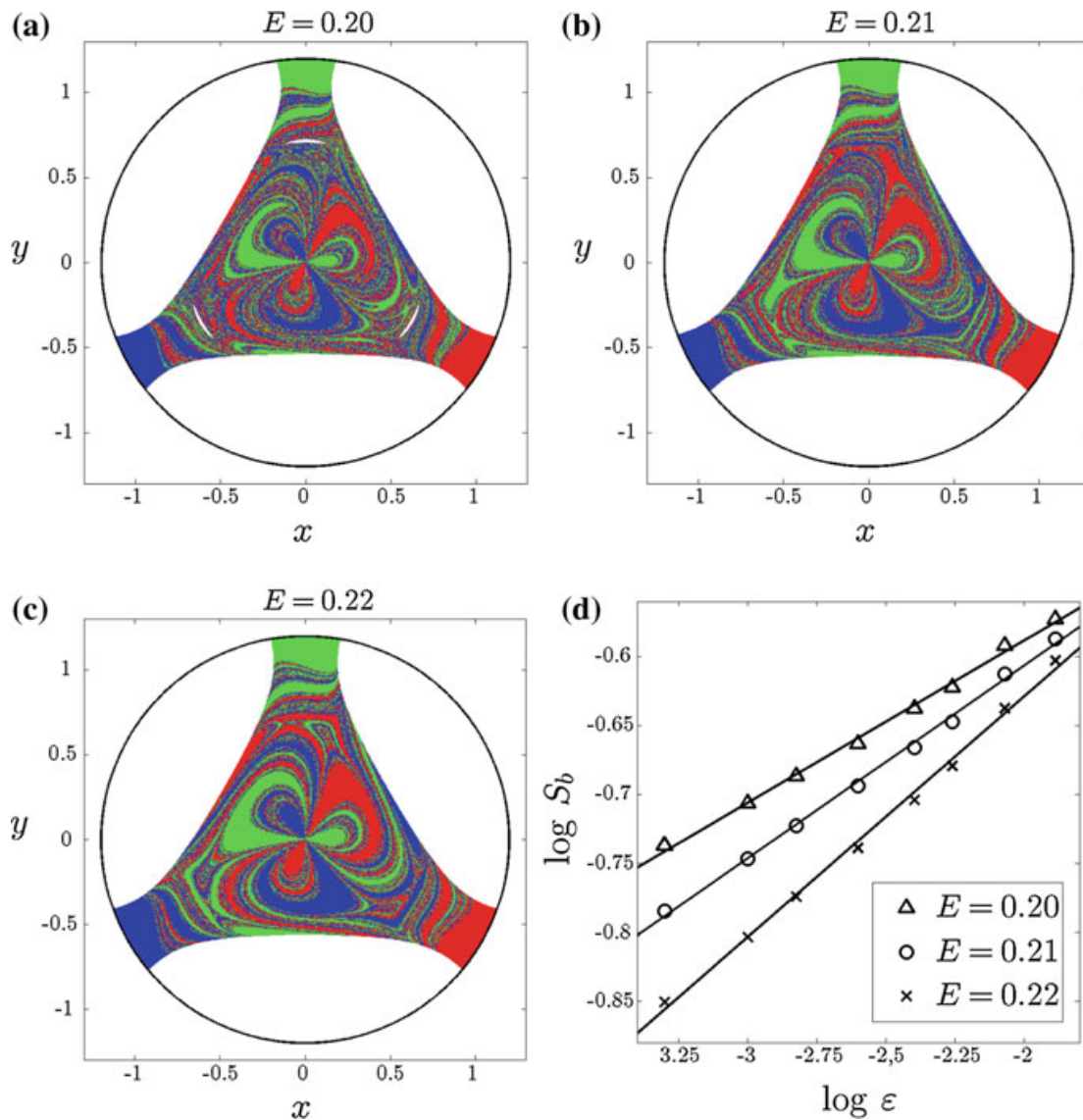


Fig. 5 Basin entropy dependence on the uncertainty exponent. a–c Escape basins of the Hénon-Heiles Hamiltonian (Eq. 9) for different values of the energy E . Inside the circles the proportion of red, blue and green boxes is always equal to $1/3$. However, as E increases the boundary becomes less uncertain, so that we can intuitively see that basin (a) is more unpredictable than basin (c). This intuition is confirmed quantitatively by the computation of the basin entropy in the log-log plot of panel (d). The most remarkable effect observed in the fits is that the slopes change because of the different dimensions of the boundaries, as expected. This effect cannot be isolated since the offsets also vary. Finally, for coarse-grained basins the basin entropy is almost equivalent

scaling of the basin entropy with box size directly reflects the fractal dimension of the basin boundaries. For small box sizes this effect dominates and the largest fractal dimensions of the basins gives the largest basin entropies, even though the offsets are different (see Fig. 5).

The last factor that contributes to the basin entropy, according to Eq. 5, is the number of attractors N_A . In general, as the number of attractors increases, the uncertainty increases too, and so does the basin entropy. Furthermore, it is impossible to isolate

the effect of the number of attractors from the contribution of the boundary size, since they are not independent: if a new attractor emerges while tuning a parameter, a new boundary is also created. We illustrate these effects using a simple map where the number of attractors can be tuned. This map comes from the Newton method to find the complex roots of unity $z^r = 1$ [20], and can be written as

$$z_{n+1} = z_n - \frac{z^r - 1}{r z^{r-1}}. \quad (10)$$

From Eq. 8 we can predict that increasing the number of attractors increases the offset in the log-log plot of the basin entropy versus the box size. This can be observed in Fig. 6, where an increasing number of attractors leads to an increasing value of the basin entropy for all the ε considered.

1.5 Basin Entropy Parameter Set

One of the most interesting applications of the basin entropy is to use it as a quantitative measure to compare different basins of attraction. We propose an analogy with the concept of *chaotic parameter set* [21], which is a plot that visually illustrates in a parameter plane when a dynamical system is chaotic or periodic by simply plotting the Lyapunov exponents for different pairs of parameters. Here, first we choose a given scaling box size ε , and then we evaluate the basin entropy associated to the corresponding basins of attraction for different parameter settings. We call the plot of the basin entropy in a two-dimensional parameter space *basin entropy parameter set*. To illustrate the possibilities of this technique, we study the periodically driven Duffing oscillator

$$\ddot{x} + \delta\dot{x} - x + x^3 = F \sin \omega t, \quad (11)$$

whose dynamics can be very different depending on the parameters. We vary the forcing amplitude F and the frequency ω of the driving, and for each basin we compute its corresponding basin entropy. We have used a resolution of 200×200 boxes ($\varepsilon = 0.005$) with 25 trajectories per box (a million trajectories per basin) to compute the basins of attraction and the same region of the phase space $\Omega = [-2.5, 2.5] \times [-2.5, 2.5]$ for all the pairs (F, ω) .

The result is presented in Fig. 7a, which is a color-code representation of the basin entropy in the parameter plane (F, ω) for different values of the forcing amplitude and frequency. The *hot* colors indicate higher values of the basin entropy, while the white pixels are for zero basin entropy. The set of parameters with zero basin entropy indicates that the basin of attraction has only one attractor. Although there is no uncertainty about the final attractor of any initial condition, trajectories may still be very complicated if the attractor is chaotic. This is actually the case for Fig. 7b, where there is only one chaotic attractor.

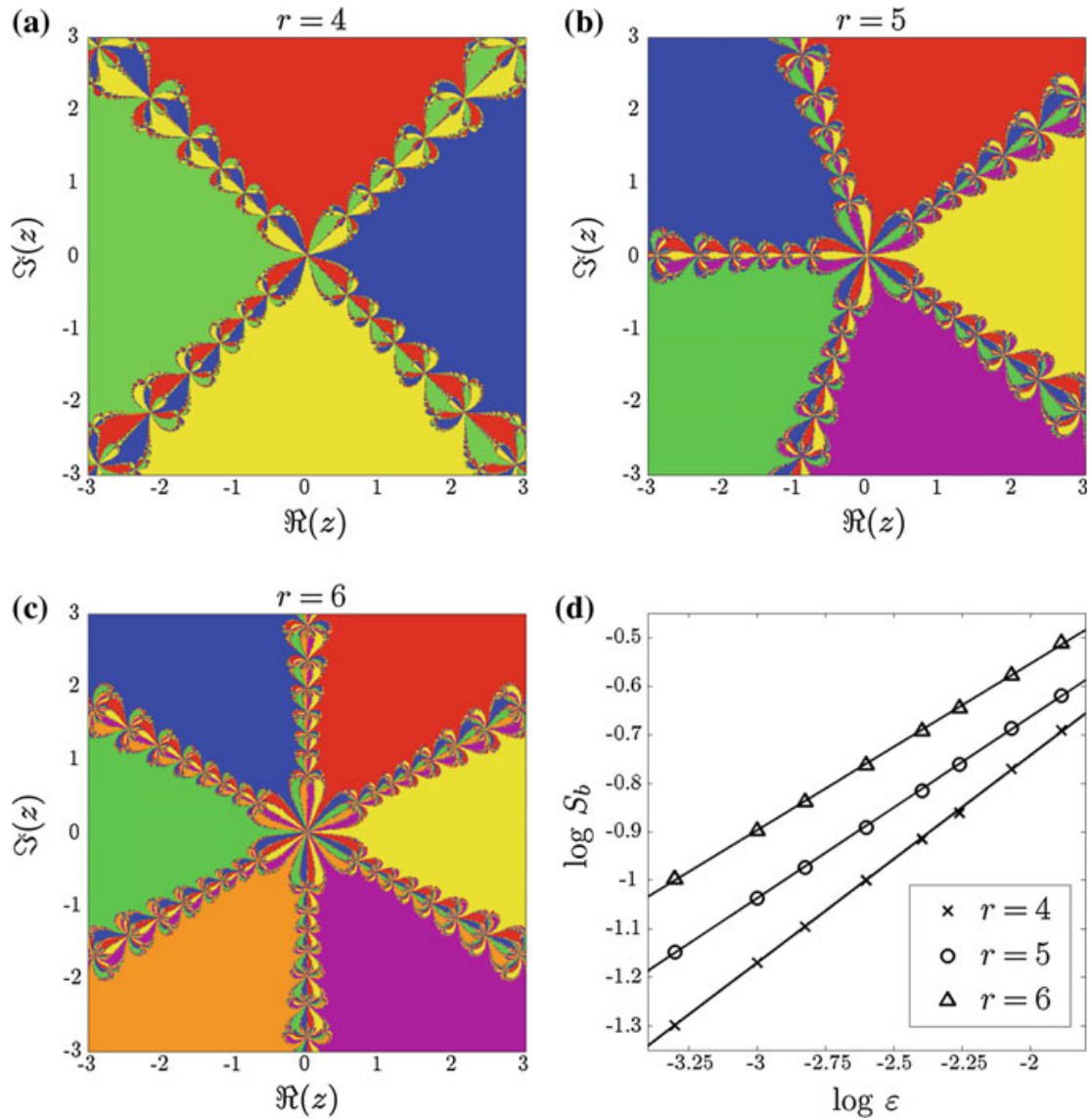


Fig. 6 Basin entropy dependence on the number of attractors. a–c The basins of attraction indicate the initial conditions that lead to the complex roots of unity using the Newton method described by $z_{n+1} = z_n - \frac{z^r - 1}{rz^{r-1}}$. Here we plot the cases $r = 4, 5, 6$. The log-log plot of panel (d) shows that the basin entropy increases when the number of attractors increases, leading to larger values in the intercepts of the fits as predicted. Nevertheless, the effect of the increasing number of attractors is impossible to separate from the other contributions to the basin entropy, since the boundaries change with the number of attractors

The *hottest* point of the basin entropy parameter set corresponds to the basin of attraction shown in Fig. 7c with eight different attractors whose basins are highly mixed. The reason for having this high value of the basin entropy lies at a combination of a high number of attractors and the uncertainty exponent associated to the boundaries that makes basins of attraction more unpredictable. In Fig. 7d, we can see a basin of attraction with extremely mixed basins, but it has only three attractors so its basin entropy is lower than for Fig. 7c. The converse situation arises in Fig. 7e, where there are sixteen different attractors but the boundaries are not very intricate.

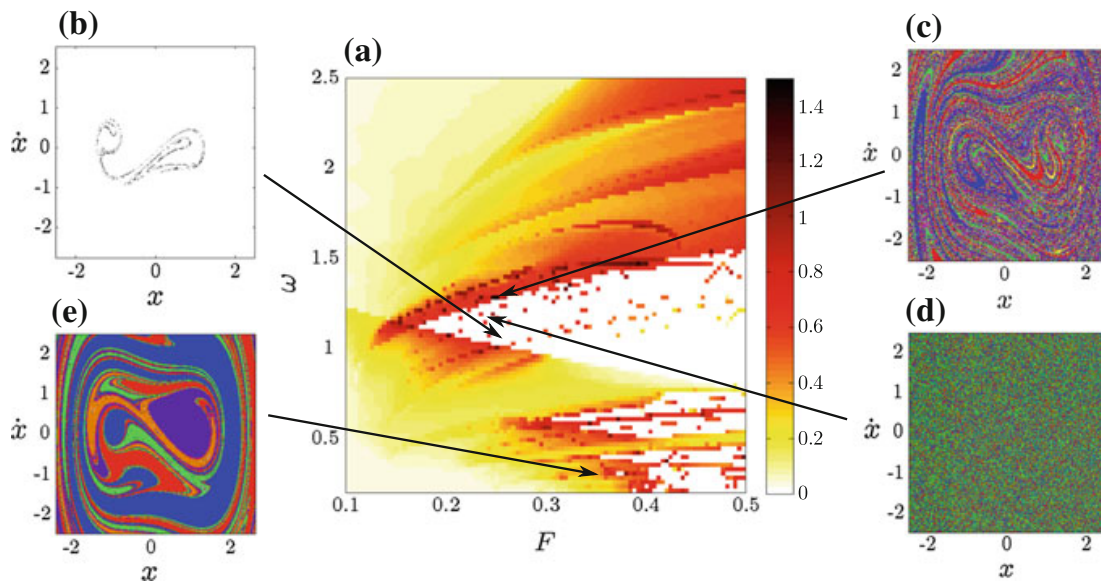


Fig. 7 Basin entropy parameter set. **a** Basin entropy parameter set for the periodically driven Duffing oscillator (Eq. 11). It is a color-code map of the basin entropy for different values (F, ω) of the forcing amplitude and frequency, where we have fixed the scaling box size $\varepsilon = 0.005$ and the damping coefficient $\delta = 0.15$. We have used a color code where the *hot* colors represent larger values of the basin entropy. **b** Example of a basin of attraction with zero basin entropy because there is only one attractor, actually a chaotic attractor (whose Poincaré section is plotted in black), for the parameters $F = 0.2575$ and $\omega = 1.075$. **c** Basins of attraction corresponding to the highest value of the basin entropy in this parameter plane, for $F = 0.2495$ and $\omega = 1.2687$. **d** Basins of attraction with three attractors and a very low uncertainty exponent corresponding to $F = 0.2455$ and $\omega = 1.1758$. **e** Basins of attraction with sixteen different attractors for the parameters $F = 0.3384$ and $\omega = 0.2929$

2 Application of Basin Entropy to Experiments with Cold Atoms

In this section, we show how the basin entropy can be used to characterize the chaotic dynamics of the system and to demonstrate the presence of fractal structures in phase space. All the results presented here are numerical experiments, but we also describe how to perform such experiments in real settings.

2.1 Cold Atoms and the Crossed Beam Configuration

In the past few years, beam splitters for guided propagating matter waves were thoroughly investigated in the thermal regime [22–26]. More recently, the Bose-Einstein condensate regime was explored using optical waveguides [27, 28]. Despite the quantum nature of these systems, some results could be understood using classical mechanics. For instance, a classical approximation was employed to unveil the chaotic dynamics underlying the experimental results in Ref. [28]. Positive Lyapunov

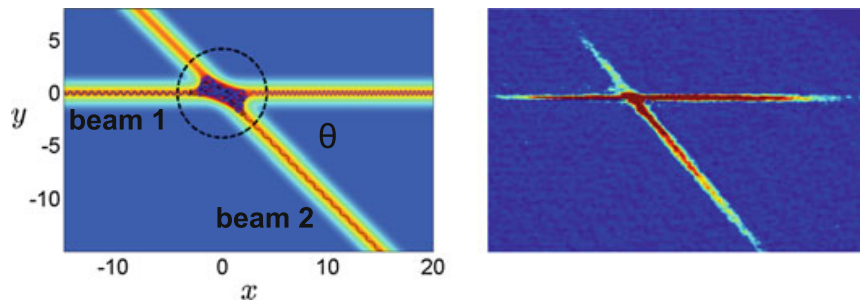


Fig. 8 The crossed beam configuration. On the left, two classical trajectories of the Hamiltonian defined by Eq. 12 with parameters $\alpha_1 = \alpha_2 = \beta_1 = \beta_2 = 1$, $\theta = 45^\circ$. The dashed circle represents the scattering region $\sqrt{x^2 + y^2} < 3\sigma$, with $\sigma = \sqrt{\frac{2}{\beta_i}}$. On the right, an experimental absorption image of the crossed beam configuration in the splitter regime ($\alpha_2/\alpha_1 \approx 1$). Hot colors indicate atoms escaping through the four different exits

exponents, a hallmark of chaos, were also estimated from experiments with ultra-cold atoms [27]. Here we exploit the concept of basin entropy to characterize this kind of systems and, more importantly, we explain how to use basin entropy in real experiments with cold atoms.

For concreteness, we focus in the configuration experimentally investigated in Refs. [25–28]. In these experiments, atoms are moving into two crossed waveguides (see Fig. 8). For the sake of simplicity, we shall use a two-dimensional model that captures the main features of the experimental system [28, 29]. Using some general assumptions [30], the motion of the particles in the Gaussian potential of the laser beams can be described by the following Hamiltonian,

$$H = \frac{1}{2} (\dot{x}^2 + \dot{y}^2) - \alpha_1 e^{-\beta_1 y^2} - \alpha_2 e^{-\beta_2 (x \sin \theta + y \cos \theta)^2}. \quad (12)$$

The features of each laser beam are condensed into two characteristic parameters: α , related to the depth of the potential and β , related to the laser waist. Along this work, we will use $\alpha_i = \beta_i = 1$.

Figure 8a shows two examples of a classical trajectory of this Hamiltonian. In Fig. 8b we can see an absorption image where a cloud of atoms is scattered, and we can measure the population of atoms in each branch. The coupling of the longitudinal and the transverse degrees of freedom that occurs at the crossing region is responsible for the complex dynamics. Surprisingly, as shown in [28], the classical description can account for the experimental results. The physical reasons are twofold: (1) the typical scale of variation of the potential is large compared to the de Broglie wavelength associated with the incoming velocity, and (2) interference effects were marginal because of the relatively short time that the wave packet spends in the scattering region, and the 3D dynamics limiting the overlap of the packet with itself. In the following, we shall investigate the fractal properties of this system using a tiling of the classical phase space. The results presented here remain pertinent for the experiments once the phase space cells considered for the statistical analysis are significantly larger than \hbar .

If we fix the shooting distance x_0 , and consider v_{x_0} and θ as parameters we can analyze the dynamics in terms of (y_0, v_{y_0}) . The set of initial conditions (y_0, v_{y_0}) that yields an escape through a given exit is referred to as an escape basin [17]. Given the Gaussian profile of the potentials, we define unbounded trajectories as those going further than $3\sigma_i$ of each laser beam $i = 1, 2$, with $\sigma_i = \sqrt{\frac{2}{\beta_i}}$. An example of such a scattering region is delimited in Fig. 8a by dashed lines. Graphical representations of escape basins are provided in Fig. 9b–d, where each color represents an exit according to the color code of Fig. 9a. White pixels are for trajectories associated to atom losses (because of the finite depth of the potential) and also for what we call sticky trajectories, i.e., that spend more than 2×10^6 time steps without escaping. These two kinds of trajectories will not be considered for the calculations of the basin entropy due to their negligible influence. Their corresponding basin is however interwoven with the other basins but it is only important for extremely low values of v_{y_0} and large initial transverse positions y_0 . In the following, we will restrict our study to the parameter ranges $v_{y_0} \in [-1.5, 1.5]$, $y_0 \in [-1.5, 1.5]$.

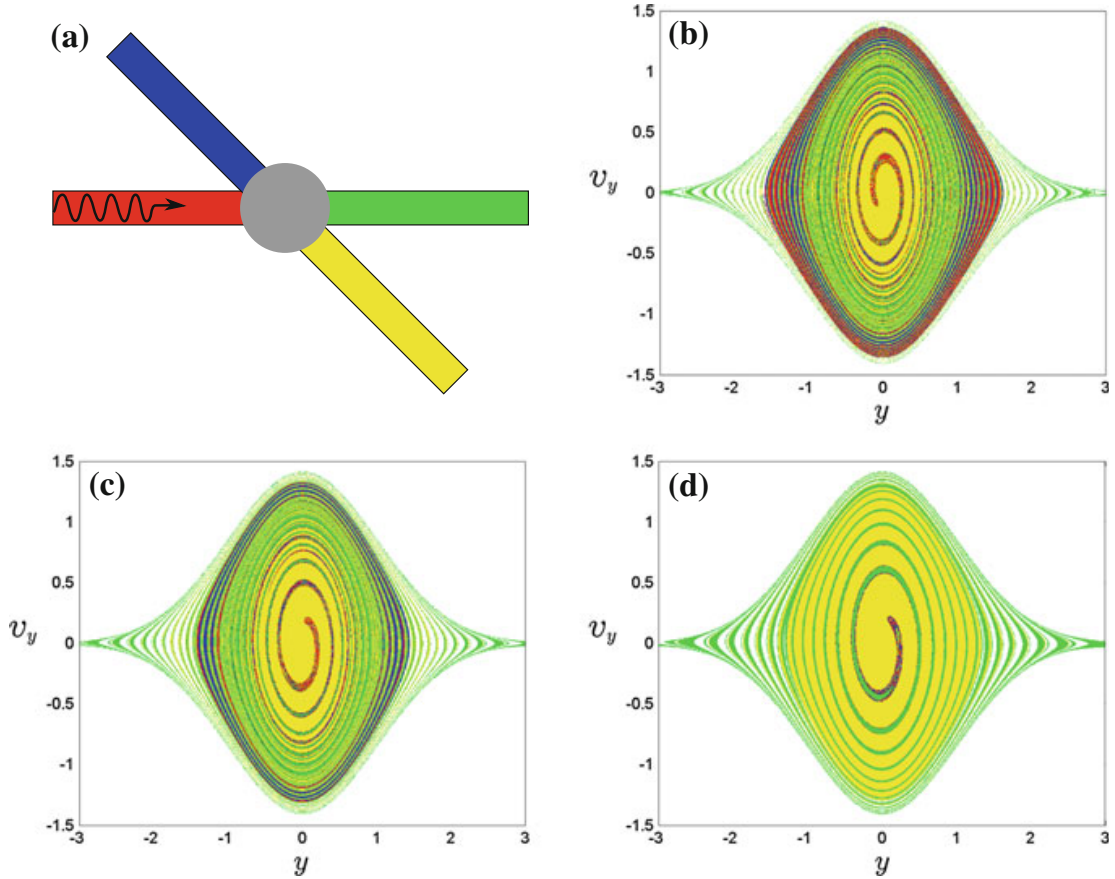


Fig. 9 Escape basins for the crossed beam configuration. The parameters for these basins are $\theta = 45^\circ$, $x_0 = -50$, $\alpha_1 = \alpha_2 = \beta_1 = \beta_2 = 1$ in Eq. 12. **a** Color code for the escape basins. **b–d** Escape basin for a shooting speeds $v_{x_0} = 0.2, 0.5, 0.8$ respectively. Basins are *less fractalized* (they have smaller basin entropy) as the shooting speed v_{x_0} increases

The presence of fractal structures is noticeable for low speed basins (see Fig. 9b), but harder to appreciate in the case of high speed, e.g., Fig. 9d. Quantifying the different *degrees of fractality* can be done with the help of the basin entropy.

2.2 *How to Compute Basin Entropy from Experimental Cold Atom Data*

The scattering experiments with cold atoms and the procedure to calculate the basin entropy share significant similarities. In both cases we consider ensembles of trajectories instead of individual trajectories. In the experiments we have clouds of atoms with different values of position and velocity, and for the basin entropy calculation we must compute many trajectories with different initial conditions inside every box. Scattering experiments essentially study the output of the trajectories in order to gain knowledge about the system, just as the basin entropy does. We propose to use as the equivalent of boxes in the basin entropy scheme, wave packets of atoms which are fired towards the scattering region. Indeed, these wave packets correspond to a group of atoms distributed around a mean value of the velocity and the position following a Gaussian distribution. The experimental measurement through absorption pictures (see Fig. 8b) provides access to the population of different branches, and thus to the probabilities inside every box.

As described in Ref. [30], we must pay attention to some technical details concerning the basin entropy computation in scattering problems. Nonetheless, in the experiments we have described these issues can be easily tackled. First, the distributions of the clouds of atoms must be in a stationary regime before arriving to the scattering region. This can be achieved varying the launching distance x_0 appropriately. Second, the basin entropy is a statistical measure, so that we need a sufficient number of initial conditions per box to get accurate values for the probabilities of the different colors. But the number of trajectories in each box is directly related to the number of atoms in a wave packet, which in real experiments is in the thousands providing excellent statistics. In fact, it could be further increased by repeating the experiment for a wave packet with same initial mean values.

Remarkably, the Monte Carlo sampling of phase space can be done experimentally by selecting different sets of initial conditions with different mean velocity v_{y_0} and mean position y_0 . In practice, small clouds of atoms will be successively delivered from a trap that accommodates a reservoir of atoms such as a Bose-Einstein condensate placed upstream. The transverse position for outcoupling the atoms can be tuned by modifying with optical means the reservoir trap geometry, while the mean transverse velocity can be transferred to the packet of atoms by applying a well-calibrated transverse magnetic gradient pulse. The successive repetition of such outcoupling procedures until the reservoir is empty permits to reduce drastically the number of experimental runs. We have checked numerically that for a realistic number of experimental runs ($N \sim 50$) the relative error in the basin entropy computation is below 10% [30].

Another important point is the size of the boxes used in the basin entropy computation, that is, the minimal resolution that can be reached in this experimental procedure. This corresponds to the size of the wave packet relative to the size of the range of phase space that we want to explore. Using experimental settings available at present time, a linear resolution of several tens can be obtained up to a maximum of one hundred [30]. This means that the experimental escape basins would have a resolution between 10×10 and 100×100 in practice.

In short, to compute the basin entropy S_b in the crossed beam configuration, one should perform a sufficient number of experiments. Each of these experiments consists in sending a wave packet with some mean transversal velocity and position. The experiments must be carried out for sufficiently long launching distances to assure the stationarity of the distributions. Then, the population escaping through each channel should be measured by absorption images. Each experimental run provides a value of the basin entropy in a box S_i . With an appropriate sampling of the region of phase space considered, the total basin entropy can be computed by averaging the basin entropy associated to each run.

2.3 *Detecting Fractal Structures in Experiments with Cold Atoms*

In this section, we investigate transient chaos and fractal structures appearing for low values of the horizontal velocity v_{x_0} . A low speed implies that particles spend more time in the scattering region, i.e., the crossing region of the two beams. Therefore, the exponential divergence of trajectories induced by the intricate shape of the potential at the crossing makes the system difficult to predict. The basin entropy captures this strong unpredictability due to the *highly fractalized* phase space. We have used a numerical Monte Carlo procedure to sample the basin entropy S_b for different shooting speeds v_{x_0} (see Fig. 10a). We can see that the basin entropy is lower for higher speeds, providing us a quantitative basis to our intuition: it is easier to predict the final destination of particles with high speed v_{x_0} . Indeed, the basin entropy seems to approach zero for very high launching speeds, where almost all the particles escape through the same exit.

In order to study the fractal nature of the basin boundaries, it is convenient to introduce the idea of *boundary basin entropy*, which can be defined as

$$S_{bb} = \frac{\sum_{i=1}^{N_b} S_i}{N_b}, \quad (13)$$

where $N_b < N$ is the number of boxes containing more than one color, that is, the number of boxes falling in the boundaries.

Using the boundary basin entropy S_{bb} we can derive a useful criterion to detect fractal boundaries in experiments. For the demonstration of this criterion we will

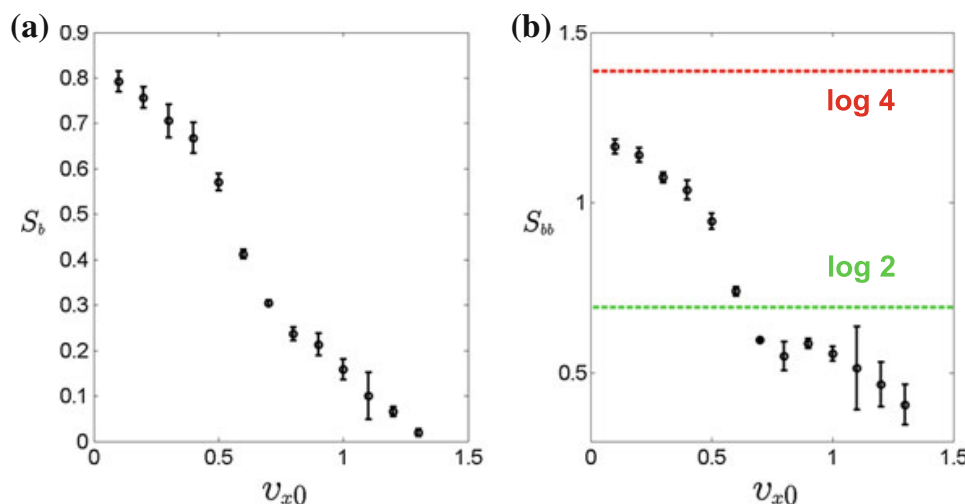


Fig. 10 Basin entropy computation using different values of the launching speed. The volume of the phase space investigated is $v_{y0} \in [-1.5, 1.5]$, $y_0 \in [-1.5, 1.5]$, $x_0 \in [-760, -750]$. For each mean value of $\langle v_{x0} \rangle$ we consider that $v_{x0} \in [\langle v_{x0} \rangle - \langle v_{x0} \rangle / 10, \langle v_{x0} \rangle + \langle v_{x0} \rangle / 10]$. The basin entropy S_b is computed using 100 boxes (experimental runs) for each represented point, and this procedure is repeated three times so that we get the error bars displayed in the figures. **a** As we increase the horizontal speed v_{x0} the basin entropy decreases. **b** The boundary basin entropy S_{bb} is above the $\log 2$ threshold (dashed line) for low speeds v_{x0} , and is below for high speeds

proceed by denying the premise, so that first we assume that our basins are separated by smooth basins. In this case, we have $\alpha = 1$, which means that the number of boxes lying in the boundary that separates two basins (boxes with two colors) grows as $N_2 = n_2 \varepsilon^{-(D-1)}$, where D is the dimension of the phase space. For $D = 2$, the boundary between two basins is a smooth line, for $D = 3$, the boundary separating two basins is a smooth surfaces and so forth.

However, if we have more than two basins, there might be some boxes N_k lying in the boundaries of $k > 2$ different basins. These boxes are in the intersection of at least two subspaces of dimension $D - 1$, that is, they are the intersection of two smooth boundaries. For instance, when $D = 2$, two or more smooth curves intersect in a point or collection of points, and when $D = 3$, two or more smooth surfaces intersect forming smooth curves. Thus, the dimension of the subspace separating more than two basins must be $D - 2$, and the boxes N_k belonging to this subspace must grow as $N_k = n_k \varepsilon^{-(D-2)}$.

Taking into account that the total number of boxes needed to cover the phase space grows as $N = \tilde{n} \varepsilon^{-D}$, we can express N_2 in terms of N as

$$N_2 = n_2 \left(\frac{N}{\tilde{n}} \right)^{\frac{D-1}{D}}, \quad (14)$$

and for the boundary boxes separating more than two basins N_k , we have

$$N_k = n_k \left(\frac{N}{\tilde{n}} \right)^{\frac{D-2}{D}}. \quad (15)$$

At this point, we recall that the maximum possible value of the entropy in a box S_i with m_i different colors is $S_i = \log m_i$, which is the Boltzmann expression for the entropy of m_i equiprobable microstates. Then, we can find that all the boxes in the boundary of two basins have $S_i \leq \log 2$, while for boxes in the boundary of k basins, $k > 2$, we have that $S_i \leq \log k$. Notice that the equality of the previous equations is only possible in pathological cases where all the boxes in the boundaries have equal proportions of the different colors.

Then, the boundary basin entropy S_{bb} for our hypothetical system with smooth boundaries is

$$S_{bb} \leq \frac{N_2 \log 2 + N_k \log k}{N_2 + N_k}. \quad (16)$$

After substituting N_2 and N_k using Eqs. 14 and 15 we get the following expression

$$S_{bb} \leq \frac{n_2 N \log 2 + n_k \tilde{n} \log k}{n_2 N + n_k \tilde{n}}, \quad (17)$$

where \tilde{n} , n_2 , n_k are constants. Finally, we can take the limit of the previous inequality for a large number of boxes, that is when $N \rightarrow \infty$, leading to

$$\lim_{N \rightarrow \infty} S_{bb} \leq \log 2. \quad (18)$$

Therefore, we have proven that if the boundaries have uncertainty exponent $\alpha = 1$ (smooth boundaries), then $S_{bb} \leq \log 2$. This is equivalent to say that if $S_{bb} > \log 2$, then $\alpha < 1$, i.e., the boundaries are fractal. This is known as the log 2 criterion.

This criterion is especially useful for experimental situations where the resolution cannot be arbitrarily chosen. In these cases we have a fixed value $\varepsilon > 0$. Nevertheless, if we take a sufficient large number of boxes N , then the log 2 criterion holds. Moreover, the equality of Eq. 18 never takes place, so that there is some room for the possible deviations caused by the impossibility of making an infinite number of simulations or experiments.

The log 2 criterion is a sufficient but not necessary condition for fractality: some fractal basins do not pass this criterion, for instance those having only two outcomes. In the case of the double beam configuration for the scattering of cold atoms, the system presents four possible exits, and for low speeds the values of S_{bb} largely exceed the log 2 threshold, as shown in Fig. 10b. Furthermore, we can see that for very small values of the launching speed the S_{bb} approaches its maximum value for this system which is log 4. This can be seen as an asymptotic value similar to systems where exits get smaller [31], since for the limiting value $v_{x_0} = 0$ the particle would never escape. We have also checked in numerical experiments that the log 2 criterion can be fulfilled for all the angles θ (except the limit cases $\theta = 0^\circ, 90^\circ$) as shown in

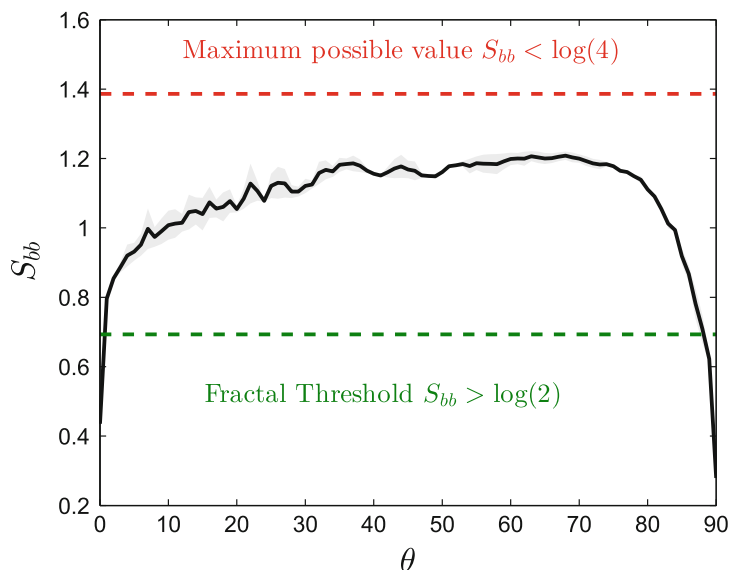


Fig. 11 Log 2 criterion and the angle of the beams. The boundary basin entropy S_{bb} is computed for different angles θ . The region of initial conditions sampled is $v_x \in [0.09, 0.11]$, $x \in [-250, -200]$, $v_y \in [-1.5, 1.5]$, $y \in [-1.5, 1.5]$. The black line is for a computation made with 100 boxes composed of 5^4 trajectories each one, and the shaded region is the absolute error with respect to an asymptotic value taken at 800 boxes. We can see that the log 2 criterion is fulfilled for all the angles except the limit cases $\theta = 0^\circ, 90^\circ$

Fig. 11. If such values were obtained in real experiments, it could be considered an experimental demonstration that the phase space is fractal.

Nevertheless, it is important to recall that the log 2 criterion detects fractals *at a given resolution*. Indeed, given a finite resolution it is impossible to distinguish a real fractal from something which is not a fractal, but that looks like it at that resolution. The log 2 criterion presents a major advantage compared to other techniques like implementing directly the box-counting algorithm: it avoids the use of different scales of velocity and position, which, in the context of experiments and in particular with cold atoms, is fundamental. The log 2 criterion is a strong argument to test fractal structures using minimal requirements. Of course, we will detect fractal structures at the resolution that can be achieved in the experiments, which depends on the size of the wave packet compared to the size of the region of phase space considered.

Finally, it is remarkable that some escape basins are not only fractal, but also may possess the stronger property of Wada [15, 16]. This means, that all the basins have a common boundary separating them. The experimental evidence of the Wada property would be that in this regime every time that more than one branch is populated, all the branches are populated. If the experiment is in the Wada regime, we will never detect atoms escaping through only two or three different branches.

3 Other Tools from Nonlinear Dynamics Applied to the Chaotic Scattering of Cold Atoms

In previous sections we have shown how the basin entropy can be very useful to characterize the unpredictability in experiments with cold atoms. Now we discuss how other methods like the basin stability allow to predict the efficiency of the switch and splitter regimes in a cross beam configuration. The escape time distribution can also be obtained and gives access to the dynamical evolution of the system. All these proposals can be implemented with current experimental techniques.

3.1 Splitter and Switch Regimes

Incident particles with high initial horizontal speed spend less time in the scattering region and most of them tend to escape through exits in the positive x direction. As a consequence, their asymptotic behavior is easier to predict, implying a decrease of the basin entropy for high $v_x(t = 0)$ (see Fig. 10a). Despite the fact that the phase space is still fractal, the $\log 2$ criterion is no longer fulfilled, as shown in Fig. 10b. This happens because there are dominant basins occupying most of the phase space, and the number of boxes lying in the boundaries decreases (see Fig. 10c).

Nevertheless, the appearance of a dominant basin is crucial for the efficiency of the switch regime, an experimental regime where we try to get as much atoms as possible escaping through the second beam. The basin entropy can give us a clue to find the parameters for this switch regime: if most particles escape through an exit, then the basin entropy must be low. Then, we can also apply the basin stability [9] to fully characterize the efficiency of the switch. The basin stability is simply the portion of phase space occupied by each basin, so $B_{Si} \in [0, 1]$ for $i = 1, \dots, 4$ and $\sum_{i=1}^4 B_{Si} = 1$. Therefore, computing the basin stability for the exit basin 2 is equivalent to calculate its efficiency. In cold atom experiments the basin stability can be computed using the same Monte Carlo sampling method used for the basin entropy computation.

Some angles like $\theta = 33^\circ$ display a large switch efficiency for high speeds, as shown in Fig. 12a. This prediction could be checked in real experiments. We have also tested the robustness of these results against small perturbations of the laser parameters ($\alpha_1, \alpha_2, \beta_1, \beta_2$). Sometimes in chaotic dynamics small perturbations of the system parameters may lead to different dynamical behaviors [21]. However this is not the case here, and the switch regime turns out to be robust against perturbations of the wave guide parameters.

In the splitter regime, we try to get approximately half of the atoms escaping through the first beam and the other half through the second beam. Using the basin stability, we can define the efficiency of the switch regime as the correlation between basin stability of exits 1 and 2, which can be calculated as their normalized product $c = 4B_{S1}B_{S2}$, where the factor 4 is to normalize at the maximum correlation value

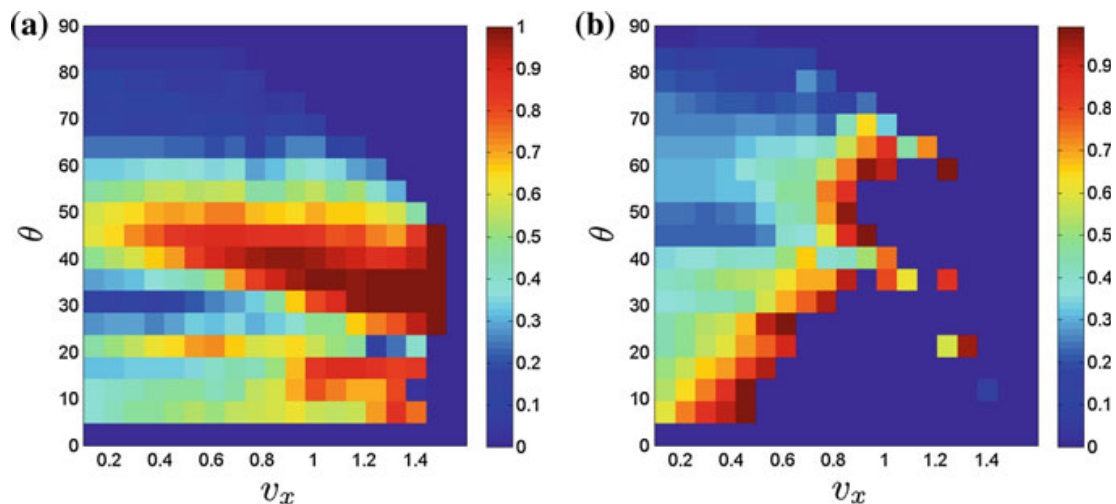


Fig. 12 Efficiency of the switch and splitter regimes. **a** Color map representing the fraction of trajectories escaping through exit 2, that is, the efficiency of the switch regime. For these computations we have used initial conditions in the region $v_y \in [-0.5, 0.5]$, $y \in [-0.5, 0.5]$ and $x_0 = -250$. **b** Color map for the correlation of the basin stability of exits 1 and 2, defined as the normalized product of their basin stability $c = 4B_{S1}B_{S2}$. For values close to 1 the system is close to a perfect 50-50 splitter regime. This takes place for larger angles as the speed increases

of $B_{S1} = B_{S2} = 0.5$. This efficiency of the splitter c is calculated for different v_x and θ and represented in Fig. 12b. We can see that as the horizontal speed v_x is increased, the splitter regime happens for larger angles. The splitter is more sensitive to perturbations of the parameters than the switch regime, as can be inferred from the non-trivial structure of Fig. 12b.

3.2 Survival Probability

The experimental setup described in Ref. [28] allows to measure not only the atom population of the branches, but also the population that lies in the crossing region for some time. Therefore, we can define the escape time as the time spent by atoms in a region of radius 3σ centered in $(0, 0)$, which we call the scattering region. We also define the survival probability as the probability P of finding an atom at a time t in the scattering region, which exactly corresponds with the measurements made in experiments.

Depending on the hyperbolic or non-hyperbolic nature of the system, the survival probability is expected to present exponential or algebraic decay for long times. In numerical simulations, we normalize time dividing by $t_0 = x/v_{x_0}$, which is the time that a particle would take to cross the scattering region if there were only one laser, and we find curves of probability versus time like the ones depicted in Fig. 13. The first plateau of this curve reflects that all the particles take at least $t = t_0$ to escape the scattering region. After the plateau, we can see an exponential decay for short times

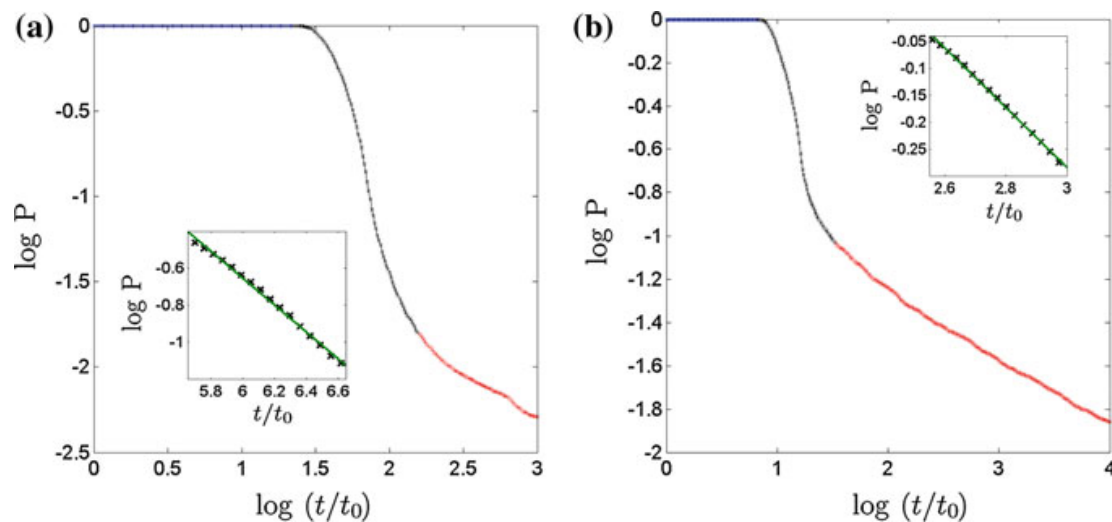


Fig. 13 Survival probability as a function of time. The survival probability P of the atoms in the scattering region as a function of time. After the initial plateau (in blue), there is an exponential decay (see inset) and for very long times an algebraic decay (in red). **a** $v_x = 0.3$. **b** $v_x = 0.9$. The rest of parameters are $\theta = 45^\circ$, $v_y \in [-0.5, 0.5]$, $y \in [-0.5, 0.5]$ and $x_0 = -250$

(see insets of Fig. 13). For very long times the decay is algebraic, a typical behavior of non-hyperbolic systems [32]. However, in real experiments we expect to see only the exponential decay for two reasons. The first one is that non-hyperbolic systems are structurally unstable [33, 34]. This means that the slightest perturbation provokes the change from algebraic to exponential decay for long times. The second reason is that in real experiments, the long time behavior is hard to follow because small atom populations are difficult to detect. Moreover, when a non-hyperbolic system is weakly perturbed the curve of probability versus time behaves as the first part of the non-perturbed system, that is, it shows an exponential decay characterized by the same mean-life τ [35].

4 Conclusions

In nonlinear dynamics, different tools are commonly used to gain knowledge of a system. For instance, Lyapunov exponents are used to characterize its dynamics. On its behalf, basins of attraction contain much information about the asymptotic behavior of the system. Some efforts had already been made in the past to characterize the complex structure of basins of attraction, such as the uncertainty exponent [7] and the notion of basin stability [9]. The uncertainty exponent takes into account the nature of the boundary between two basins, and the basin stability informs about the percentage of phase space occupied by each basin. However, in many situations these concepts are insufficient to describe the complex structure of the basins of attraction [19].

The basin entropy integrates these concepts from the theoretical perspective of information entropy. It provides a quantitative measure of the uncertainty associated to the basins of attraction for a given scaling box size. This should become a very useful tool with a wide range of applications, as exemplified by the different systems that we have used to illustrate this concept.

In particular, here we have shown how the basin entropy can be applied to investigate the dynamics of propagating matter waves. We have focused on a double guide configuration, where the atoms can escape through four different exits. So far, non-linear dynamics had only been used as an approximation to explain *a posteriori* some results concerning the chaotic dynamics of the atoms. But here we propose to go far beyond. In real experiments, we can measure the atom population escaping through each branch, that is, we can measure the probabilities of the atoms of escaping through the different exits. Gathering this information through an appropriate Monte Carlo sampling, we can measure the basin entropy for a given set of parameters. This enables the characterization of the final state unpredictability associated to different experimental parameters. Using the same data, we have shown how the presence of fractal structures in phase space could be detected for a certain ranges of parameters. An interesting modification of the experimental setting would be the inclusion of more guides. Indeed, with more exits, the $\log 2$ criterion would be more easily fulfilled, facilitating the detection of fractality.

In terms of applicability, the tools developed here can be used more systematically to investigate the efficiency and robustness of the different experimental regimes of the crossed beam configuration in order to use it reliably as part of a matter wave circuit [36]. The protocols that we propose have been designed for a direct implementation with state of the art experimental techniques.

Acknowledgements This work was supported by the Spanish Ministry of Economy and Competitiveness under Project No. FIS2013-40653-P and by the Spanish State Research Agency (AEI) and the European Regional Development Fund (FEDER) under Project No. FIS2016-76883-P. MAFS acknowledges the jointly sponsored financial support by the Fulbright Program and the Spanish Ministry of Education (Program No. FMECD-ST-2016). Financial support from the Programme Investissements d'Avenir under the program ANR-11-IDEX-0002-02, reference ANR-10-LABX-0037-NEXT is also acknowledged.

References

1. Nusse, H.E., Yorke, J.A.: *Science* **271**, 1376 (1996)
2. Aguirre, J., Viana, R.L., Sanjuán, M.A.F.: *Rev. Mod. Phys.* **81**, 333 (2009)
3. Kolmogorov, A.N.: *Doklady Russ. Acad. Sci.* **119**, 861 (1959)
4. Sinai, Y.G.: *Doklady Russ. Acad. Sci.* **124**, 754 (1959)
5. Adler, R.L., Konheim, A.G., McAndrew, M.H.: *Trans. Am. Math. Soc.* **114**, 309 (1965)
6. Hunt, B.R., Ott, E.: *Chaos* **25**, 097618 (2015)
7. Grebogi, C., McDonald, S.W., Ott, E., Yorke, J.A.: *Phys. Lett. A* **99**, 415 (1983)
8. Grebogi, C., Kostelich, E., Ott, E., Yorke, J.A.: *Phys. Lett. A* **118**, 448 (1986)
9. Menck, P.J., Heitzig, J., Marwan, N., Kurths, J.: *Nat. Phys.* **9**, 89 (2013)
10. Alexander, J., Yorke, J.A., You, Z., Kan, I.: *Int. J. Bifurcat. Chaos* **02**, 795 (1992)

11. Ott, E., Sommerer, J.C., Alexander, J.C., Kan, I., Yorke, J.A.: *Phys. Rev. Lett.* **71**, 4134 (1993)
12. Lai, Y.-C., Winslow, R.L.: *Phys. Rev. Lett.* **74**, 5208 (1995)
13. Daza, A., Wagemakers, A., Georgeot, B., Guéry-Odelin, D., Sanjuán, M.A.F.: *Sci. Rep.* **6**, 31416 (2016)
14. Alligood, K.T., Sauer, T.D., Yorke, J.A.: *Chaos: An Introduction to Dynamical Systems*. Springer, New York (1996)
15. Kennedy, J., Yorke, J.A.: *Phys. D* **51**, 213 (1991)
16. Daza, A., Wagemakers, A., Sanjuán, M.A.F., Yorke, J.A.: *Sci. Rep.* **5**, 16579 (2015)
17. Aguirre, J., Vallejo, J.C., Sanjuán, M.A.F.: *Phys. Rev. E* **64**, 066208 (2001)
18. Hnon, M., Heiles, C.: *Astron. J.* **69**, 73 (1964)
19. Blesa, F., Seoane, J.M., Barrio, R., Sanjun, M.A.F.: *Int. J. Bifurcat. Chaos* **22**, 1230010 (2012)
20. Epureanu, B., Greenside, H.: *SIAM Rev.* **40**, 102 (1998)
21. Sanjun, M.A.F.: *Phys. Rev. E* **58**, 4377 (1998)
22. Cassettari, D., Hessmo, B., Folman, R., Maier, T., Schmiedmayer, J.: *Phys. Rev. Lett.* **85**, 5483 (2000)
23. Renn, M.J., Montgomery, D., Vdovin, O., Anderson, D.Z., Wieman, C.E., Cornell, E.A.: *Phys. Rev. Lett.* **75**, 3253 (1995)
24. Müller, D., Cornell, E.A., Prevedelli, M., Schwindt, P.D.D., Wang, Y.-J., Anderson, D.Z.: *Phys. Rev. A* **63**, 041602 (2001)
25. Houde, O., Kadio, D., Pruvost, L.: *Phys. Rev. Lett.* **85**, 5543 (2000)
26. Dumke, R., Volk, M., Müther, T., Buchkremer, F.B.J., Birkel, G., Ertmer, W.: *Phys. Rev. Lett.* **89**, 097903 (2002)
27. Gattobigio, G.L., Couvert, A., Georgeot, B., Guéry-Odelin, D.: *Phys. Rev. Lett.* **107**, 254104 (2011)
28. Gattobigio, G.L., Couvert, A., Reinaudi, G., Georgeot, B., Guéry-Odelin, D.: *Phys. Rev. Lett.* **109**, 030403 (2012)
29. Torrontegui, E., Echanobe, J., Ruschhaupt, A., Guéry-Odelin, D., Muga, J.G.: *Phys. Rev. A* **82**, 043420 (2010)
30. Daza, A., Georgeot, B., Guéry-Odelin, D., Wagemakers, A.A., Sanjuán, M.A.F.: *Phys. Rev. A* **95**, 013629 (2017)
31. Aguirre, J., Sanjuán, M.A.F.: *Phys. Rev. E* **67**, 056201 (2003)
32. Lai, Y.C., Tél, T.: *Transient Chaos*. Springer, New York (2011)
33. Seoane, J.M., Sanjuán, M.A.F., Lai, Y.C.: *Phys. Rev. E* **76**, 016208 (2007)
34. Seoane, J.M., Huang, L., Sanjuán, M.A.F., Lai, Y.C.: *Phys. Rev. E* **79**, 047202 (2009)
35. Motter, A.E., Lai, Y.C.: *Phys. Rev. E* **65**, 015205 (2001)
36. Seaman, B.T., Krämer, M., Anderson, D.Z., Holland, M.J.: *Phys. Rev. A* **75**, 023615 (2007); Ryu, C., Boshier, M.G.: *New J. Phys.* **17**, 092002 (2015); Caliga, S.C., Straatsma, C.J.E., Anderson, D.Z.: *New J. Phys.* **18**, 025010 (2016)



<http://www.springer.com/978-3-319-68108-5>

Chaotic, Fractional, and Complex Dynamics: New
Insights and Perspectives

Edelman, M.; Macau, E.E.N.; Sanjuan, M.A.F. (Eds.)

2018, IX, 315 p. 118 illus., 76 illus. in color., Hardcover

ISBN: 978-3-319-68108-5